Draft version March 17, 2024
Typeset using LaTeX **twocolumn** style in AASTeX63

arXiv:2009.09954v1 [astro-ph.GA] 21 Sep 2020

Origin of Weak Mg II and Higher Ionization Absorption Lines in an Outflow from an Intermediate-Redshift Dwarf Satellite Galaxy

Akimi Fujita,[1] Toru Misawa,[2] Jane C. Charlton,[3] Avery Meiksin,[4] and Mordecai-Mark Mac Low[5,6]

[1] *Faculty of Engineering, Shinshu University, 4-17-1 Wakasato, Nagano, Nagano 380-0926, Japan*
[2] *School of General Studies, Shinshu University, 3-1-1, Asahi, Matsumoto City 390-8621, Japan*
[3] *Department of Astronomy & Astrophysics, The Pennsylvania State University, University Park, PA, 16802, USA*
[4] *SUPA[a], Institute for Astronomy, University of Edinburgh, Blackford Hill, Edinburgh EH9 3HJ, UK*
[5] *Department of Astrophysics, American Museum of Natural History, New York, NY 10024, USA*
[6] *Center for Computational Astrophysics, Flatiron Institute, New York, NY 10010, USA*

Submitted to ApJ

ABSTRACT

Observations at intermediate redshifts reveal the presence of numerous, compact, weak MgII absorbers with near to super-solar metallicities, often surrounded by more extended regions that produce CIV and/or OVI absorption in the circumgalactic medium at large impact parameters from luminous galaxies. Their origin and nature remains unclear. We hypothesize that undetected, satellite dwarf galaxies are responsible for producing some of these weak MgII absorbers. We test our hypothesis using gas dynamical simulations of galactic outflows from a dwarf satellite galaxy with a halo mass of 5×10^9 $M_\odot$, which could form in a larger L^* halo at $z = 2$, to study the gas interaction in the halo. We find that thin, filamentary, weak MgII absorbers are produced in two stages: 1) when shocked core collapse supernova (SNII) enriched gas descending in a galactic fountain gets shock compressed by upward flows driven by subsequent SNIIs and cools (*phase 1*), and later, 2) during an outflow driven by Type Ia supernovae that shocks and sweeps up pervasive SNII enriched gas, which then cools (*phase 2*). The width of the filaments and fragments are $\lesssim$ 100 pc, and the smallest ones cannot be resolved at 12.8 pc resolution. The MgII absorbers in our simulations are continuously generated for $>$ 150 Myr by shocks and cooling, though each cloud survives for only $\sim$ 60 Myr. Their metallicity is 10–20% solar metallicity and column density is $< 10^{12}$ cm^{-2}. They are also surrounded by larger (0.5–1 kpc) CIV absorbers that seem to survive longer. In addition, larger-scale ($>$ 1 kpc) CIV and OVI clouds are produced in both expanding and shocked SNII enriched gas which is photoionized by the UV metagalactic radiation at intermediate redshift. Our simulation highlights the possibility of dwarf galactic outflows producing highly enriched multiphase gas.

Keywords: galactic outflows — CGM— hydrodynamic simulations — dwarf galaxies

1. INTRODUCTION

Galactic outflows appear to regulate the structure and evolution of galaxies, as they heat, ionize, and chemically enrich the surrounding circumgalactic medium (CGM) and even drive unbound winds that can reach the intergalactic medium (IGM) (see e.g. Somerville & Davé 2015; Heckman 2017, for reviews). A robust understanding of the stellar feedback processes driving these outflows, however, remains elusive. The observed properties of the outflows and outflow-CGM interaction at multiple wavelengths must be used to constrain theoretical models of the physics governing the outflows and outflow-CGM interaction. The most prominent observed properties are metal absorption lines, seen in the spectra of background quasars, that are believed to arise from inhomogeneities in the CGM. Numerical simulations are required to predict and interpret the observational signatures of these systems (e.g. Oppenheimer

Corresponding author: Akimi Fujita
fujitaa@shinshu-u.ac.jp

[a] Scottish Universities Physics Alliance

et al. 2012; Suresh et al. 2015; Keating et al. 2016; Turner et al. 2017; Oppenheimer et al. 2018; Peeples et al. 2019).

The derived metallicities of weak, low ionization absorbers are almost always greater than 10% solar and are often as high or even higher than the solar value. Some of them are even iron-enhanced compared with solar (Rigby et al. 2002; Charlton et al. 2003; Narayanan et al. 2008; Misawa et al. 2008; Lynch & Charlton 2007). In addition, analyses of low-redshift absorbers show that there are fewer absorbers at present than in the past, and that most absorbers seem to live in group environments (Muzahid et al. 2017). With all the measured properties above, it is plausible to speculate that weak absorbers are created by transient processes, such as galactic outflows that carry metals and are less active in the modern Universe. The outflows may originate in satellite dwarf galaxies hosted by a larger halo that are too dim to be observed.

The covering fraction of the weak absorbers is estimated to be $\gtrsim 30\%$ in the CGM of galaxies brighter than $0.001L^*$(Narayanan et al. 2008; Muzahid et al. 2017). There would be on the order of a million tiny, weak absorbers per galaxy if a spherical geometry were assumed (Rigby et al. 2002). It has been argued, however, that weak absorbers reside instead in filamentary and sheet-like structures (Milutinovic et al. 2006).

Many of these systems show absorption by multiple high ionization species at the same velocity, often with additional components offset by 5-150 km s^{-1} (Milutinovic et al. 2006). CIV surveys at $z \approx 2 \sim 3$ in the environments of sub-Lyman Limit Systems (sLLS) suggest that CIV clouds are more diffuse ($n_{HI} \sim 10^{-4}$ to 10^{-3} cm^{-3}) and larger than MgII clouds, with sizes between 0.1 kpc and 10 kpc (Simcoe et al. 2004; Schaye et al. 2007; Lehner et al. 2016). Some of CIV clouds may have expanded from denser, more compact MgII clouds (Schaye et al. 2007). These CIV systems may be interpreted as being in photoionization equilibrium at $T\sim 10^4$ K, and their metallicities are found to be $\sim 1\%$ solar to even solar or more (Simcoe et al. 2004; Schaye et al. 2007; Lehner et al. 2016). There are also many OVI absorption systems, which are more likely to have an origin in photoionized gas (rather than collisionally ionized gas) at z∼2 due to the greater intensity of the EBR. The detections of OVI by Turner et al. (2014, 2015), however, suggest the presence of a collisionally ionized gas phase for impact parameters $\lesssim$100 proper kpc (pkpc) of large, star-forming galaxies at z∼ 2.4.

In this paper, we test our hypothesis that galactic outflows from satellite dwarf galaxies, too dim to detect in the halo of a larger L^* galaxy, produce compact weak MgII absorbers surrounded by larger regions that produce CIV and OVI absorption. Using a small-scale hydrodynamical simulation of a dwarf galaxy, we find such structures are produced by repeated shocks and radiative cooling in the gaseous halo of the galaxy. We will highlight important physical processes at work which regulate the production of low and high ionization clouds, to be explored in larger-scale simulations in the next paper. We describe our numerical method in Section 2 and the dynamics of SNII and SNIa driven outflows and their interaction with surrounding gas, including the production of dense clumps and filaments, in Section 3. In Section 4, we study the distributions of weak MgII absorbers and surrounding CIV and OVI absorbers in our simulation, and compare them to the properties of observed systems, followed by a resolution study (Section 5) and a summary (Section 6).

2. NUMERICAL METHOD

We use the adaptive mesh refinement hydrodynamics code Enzo (Bryan et al. 2014) to simulate repeated supernova explosions in the disk of a dwarf galaxy. We solve the equations of hydrodynamics using a direct-Eulerian piecewise parabolic method (Colella & Woodward 1984; Bryan et al. 2014) and a two-shock approximate Riemann solver with progressive fallback to more diffusive Riemann solvers in the event that higher order methods produce negative densities or energies. Our simulation box has dimensions $(L_x, L_y, L_z) = (6.5536, 6.5536, 32.768)$ kpc, initially with (32, 32, 160) cells. Only half the galactic disk above its midplane is simulated. We refine cells to resolve shocks with a standard minimum pressure jump condition (Colella & Woodward 1984) and to resolve cooling at turbulent interfaces where the sound crossing time exceeds the cooling time. We use 4 refinement levels resulting in a highest resolution of 12.8 pc (*standard simulation*). We also ran the same simulation with 3 refinement levels as a comparative resolution study (*low-res simulation*), and by applying 6 refinement levels in a region where MgII filaments form in order to test the effects of resolution on fragmentation (*high-res zoom simulation*). We assume a flat ΛCDM cosmology with the 2018 Planck Collaboration measured parameters $\Omega_m = 0.315$, $\Omega_\Lambda = 0.685$, $h = 0.674$, and $\Omega_b = 0.0493$ (Aghanim et al. 2019).

2.1. *Galaxy Model*

We model a dwarf galaxy at redshift $z = 2$ with a halo mass $M_{\rm halo} = 4 \times 10^9$ $M_\odot$, and a virial radius $R_{\rm vir} = 17.3\,{\rm kpc}$. This model has a disk gas mass, $M_{\rm g} = 5.2 \times 10^8$ $M_\odot$. We adopt a Burkert (1995) dark matter potential with a core radius $r_0 = 848\,{\rm pc}$ and

central density $\rho_0 = 1.93 \times 10^{-23}$ g cm^{-3}, although this potential profile is a fit to the observed rotation curves of nearby dwarf galaxies rather than those at z=2. Our choice of r_0 and ρ_0 ensures that the resulting potential profile reproduces a Navarro et al. (1997) dark matter potential with $c = 12.2$ for the same dwarf halo at $r > 400$ pc. The gas is described as a softened exponential disk:

$$\rho(R,z) = \frac{M_{\rm g}}{2\pi a_{\rm g}^2 b_{\rm g}} 0.5^2 {\rm sech}\left(\frac{R}{a_{\rm g}}\right) {\rm sech}\left(\frac{z}{b_{\rm g}}\right) \quad (1)$$

where $M_{\rm g}$ is the total mass of gas in the disk, and $a_{\rm g}$ and $b_{\rm g}$ are the radial and vertical gas disk scale heights (Tonnsen & Bryan 2009). We chose $a_{\rm g} = 621$ pc based on the exponential disk approximation of Mo et al. (1998), with $\lambda = 0.05$, and $b_{\rm g} = 160$ pc based on the thin disk approximation (Toomre 1963) with an effective sound speed, $c_{\rm s,eff} = 11.3$ km s^{-1} (Fujita et al. 2009). Given this gas density distribution in the disk, the gas temperature and pressure are calculated to maintain the disk in hydrostatic equilibrium with the surrounding halo potential in the z-direction, and the rotational velocity of the gas disk is set to balance the radial gravitational force and the pressure gradient. The disk temperature varies between 10^3 K and a few $\times 10^4$ K, and the maximum circular velocity is $v_{\rm max} = 48.8$ km s^{-1} with the escape velocity from the potential $v_{\rm esc} = 69.0$ km s^{-1}. Our model galaxy is placed in a static halo background with $\rho_{\rm bg} = 1.83 \times 10^{-28}$ g cm^{-3} so that the gas mass within the virial radius is $\mathrm{M_{halo}}\left(\frac{\Omega_{\rm b}}{\Omega_{\rm m}}\right)$. The metallicity of all the gas in the box is initially set at $Z = 0.001$ with mean molecular weight $\mu = 0.6$.

2.2. *Cooling*

Figure 1 shows the cooling curves used in our simulations. We use radiative cooling curves as a function of temperature above 10^4 K for gas in collisional ionization equilibrium (CIE) with various metallicities: [Fe/H]=-3, -2, -1.5, -1, -0.5, 0, +0.5 (Sutherland & Dopita 1993). A radiative cooling rate for gas in a cell with a metallicity is computed by interpolating between the cooling curves. Cooling of gas below temperature 10^4 K is approximated with the cooling curve of Rose & Bregman (1995) computed for solar metallicity. Although, for example, Maio et al. (2007) shows that the cooling rate stays approximately the same between 10^3 and 10^4 K for gas with a metallicity below $Z = 10^{-3}$, we justify the simplification below 10^4 K by noting that cooling below 10^4 K has a negligible effect on the formation and fragmentation of dense clouds as cooling in shocked gas and turbulent mixing layers is limited by numerical resolution rather than by radiative cooling (Fujita et al. 2009; Gronke & Oh 2018, 2020). We justify CIE assumption because past simulations show that the effects of non-equilibrium ionization (NEI) do not much boost high ion distributions even in shocked coronal gas (Kwak & Shelton 2010; Armillotto et al. 2016; Cottle et al. 2018). We do not include the effects of a metagalactic UV background radiation in our simulation, but we incorporate them when we post-process the simulations to compute the ion distributions (see Sect. 4). The modification of the ionization fraction by a UV background would affect only the lower density gas that does not dominate the cooling.

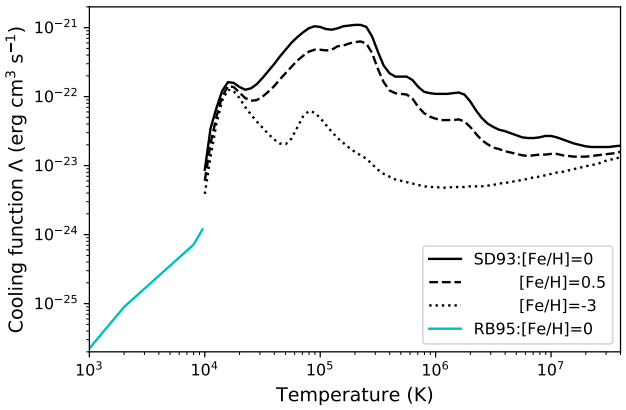


Figure 1. Radiative cooling functions used in our simulations as a function of temperature T from Sutherland & Dopita (1993) for $T \geq 10^4$ K for different metallicities and from Rose & Bregman (1995) for $T < 10^4$ K for solar metallicity.

2.3. *Starburst*

In our study, we set up an instantaneous starburst of total stellar mass 4×10^6 M$_\odot$ at the disk center. We use Stellar Yields for Galactic Modeling Applications (SYGMA Ritter et al. 2018) to model the chemical ejecta and feedback from simple stellar populations (SSPs). SYGMA is part of the open-source chemical evolution NuGrid framework (NuPyCEE[1]). We compute the average mechanical luminosities and the average metal ejection rates for $\mathrm{M_{SSP}} = 4 \times 10^6$ M$_\odot$. They are $L_{\rm SNII} = 4 \times 10^{40}$ erg s^{-1} and $\dot{M}_{\rm SNII} = 1.2 \times 10^{-3}$ M$_\odot$ yr^{-1} for the initial 40 Myr, which is the lifetime of the smallest B star to go core collapse Type II supernova (SNII), and $L_{\rm SNIa} = 8 \times 10^{37}$ erg s^{-1} and $\dot{M}_{\rm SNIa} = 1.0 \times 10^{-5}$ M$_\odot$ yr^{-1} at times ≥ 40 Myr powered by Type Ia supernovae (SNIa). The metals produced by SNII and SNIa are followed and advected separately.

[1] http://www.nugridstars.org

To drive a constant-luminosity outflow, during every time step Δt we add mass ($\dot{M}_{\rm in}\Delta t$) and energy ($L_{\rm SNII}\Delta t$ and $L_{\rm SNIa}\Delta t$) to a spherical source region with a radius of 102.4 pc. We choose to increase the amount of mass added from the SYGMA values to ensure that the temperature of hot gas in the outflows is 3×10^7 K, which is far from the peak of the cooling curve at $\sim 10^5$ K, but well below the value implied by only accounting for the ejecta. This additional mass accounts for the mass evaporated off the swept-up shells in the absence of an implementation of thermal heat conduction. Therefore, we use $\dot{M}_{\rm in} = 8.3 \times 10^{-2}$ M$_\odot$ yr^{-1} for the SNII driven outflow and 1.7×10^{-4} M$_\odot$ yr^{-1} for the SNIa driven outflow. The total mass added for 1 Gyr is only 3.48×10^6 M$_\odot$ which is less than 1% of M$_{\rm disk}$.

2.4. *Ion Analysis*

We use the TRIDENT analysis tool (Hummels et al. 2017) to calculate the ionization fractions of the species of interest based on the cell-by-cell density, temperature, and metallicity. First, the estimation for the number density of an element X is

$$n_X = n_H \frac{\rm Z}{\rm Z_\odot} \left(\frac{n_X}{n_H}\right)_\odot , \quad (2)$$

where Z is the metallicity from the simulation, and $(n_X/n_H)_\odot$ is the solar abundance by number. Ionization fractions are pre-calculated over a grid of temperature, density, and redshift in photoionization equilibrium (PIE) with the metagalactic UV background radiation by Haardt & Madau (2012), using the photoionization software CLOUDY (Ferland et al. 2013). Thus by linearly interpolating over the pre-calculated grid, TRIDENT returns the density of an ion, i, of an element, X as

$$n_{X_i} = n_X f_{X_I}, \quad (3)$$

where f_{X_I} is the ionization fraction of the ith ion.

To generate an absorption profile along a ray through the simulation box, the absorption produced by each grid cell is represented by a single Voigt profile at its instantaneous velocity v, with a Doppler b parameter specified by the temperature in the cell.

3. RESULTS

Figure 2 shows density, temperature, total velocity, and metallicity slices along the y-z plane at the disk center and a neutral hydrogen (HI) column density distribution along x axis in the y-z plane at t=40 Myr. The HI distribution is calculated with Trident.

The swept-up shell driven by repeated SNII explosions cools quickly due to its high density. Because it is expanding into a stratified atmosphere, it accelerates and fragments into multiple clumps and shells due to the Rayleigh-Taylor (RT) instability. Figure 2 shows that the hot, thermalized interior gas expands freely through the fragments, forming a supersonic, energy-driven outflow. Kelvin-Helmholtz instabilities ablate the sides of these fragments as the hot gas streams past them. This outflow continues to shock the CGM, and a classic superbubble (Weaver et al. 1977) forms in the CGM, as seen in Figure 2: region (a) expanding SNII enriched gas at v$\sim$400–1000 km s^{-1}, region (b) shocked SNII enriched gas, region (c) swept-up CGM shell which is very thin and light because there is not much to sweep due to its low density, and region (d) the ambient CGM beyond the outer shock front at z$\sim$17 kpc. Expanding SNII enriched gas and shocked SNII enriched gas are divided at the inner shock front at z$\sim$12 kpc, and shocked SNII enriched gas extends out to a contact discontinuity with the CGM.

In our simulations, the high-density, low-temperature fragments of swept-up ISM material are not resolved after $t = 40$ Myr with our refinement criteria of strong pressure gradients or the sound crossing time exceeding the cooling time. They are Lyman Limit Systems (LLSs) and sub-Damped Lyman-alpha Absorbers (DLAs) with $N_{HI} \gtrsim 10^{18-20}$ cm^{-2} that will likely produce strong MgII absorbers (see *rightmost* figure in Figure 2). The focus of this study is instead on weak MgII absorbers that are observed to be associated with sub-LLSs with $N_{HI} \lesssim 10^{17}$ cm^{-2}. These unresolved swept-up ISM fragments in the outflow quickly mix with the surrounding hot, metal enriched gas, but the total amount of disk gas mixed in the outflow is only 3–5% of the disk mass initially placed on the grid. We also note that the powerful SNII driven outflow leaves the box starting at $t \sim 20$ Myr; by $t = 40$ to 300 Myr, 38% to 58% of the metal-carrying gas has left the box.

After the last SNII goes off at $t = 40$ Myr, SNIa's drive the outflow, but with a mechanical luminosity that is more than two orders of magnitude smaller. SNIa-enriched gas expands at $v \sim 400$ km s^{-1} through the tunnel created by the previous SNII outflow, but by $t \sim 80$ Myr the disk gas being pushed aside by the SNII outflow flows back to the central source region, blocking the passage for SNIa-enriched gas. Meanwhile, the shocked SNII-enriched gas (region b) near the inner shock front ($z \sim 12$ kpc) begins to descend toward the disk, while the outer shock front (the outer edge of region c) keeps moving at $v \sim 400$ km s^{-1} in the CGM and soon leaves the box. By $t \sim 100$ Myr, descending shocked SNII enriched gas accumulates at the inner shock front and cools to form denser, cool shells that eventually fragment by RT instability.

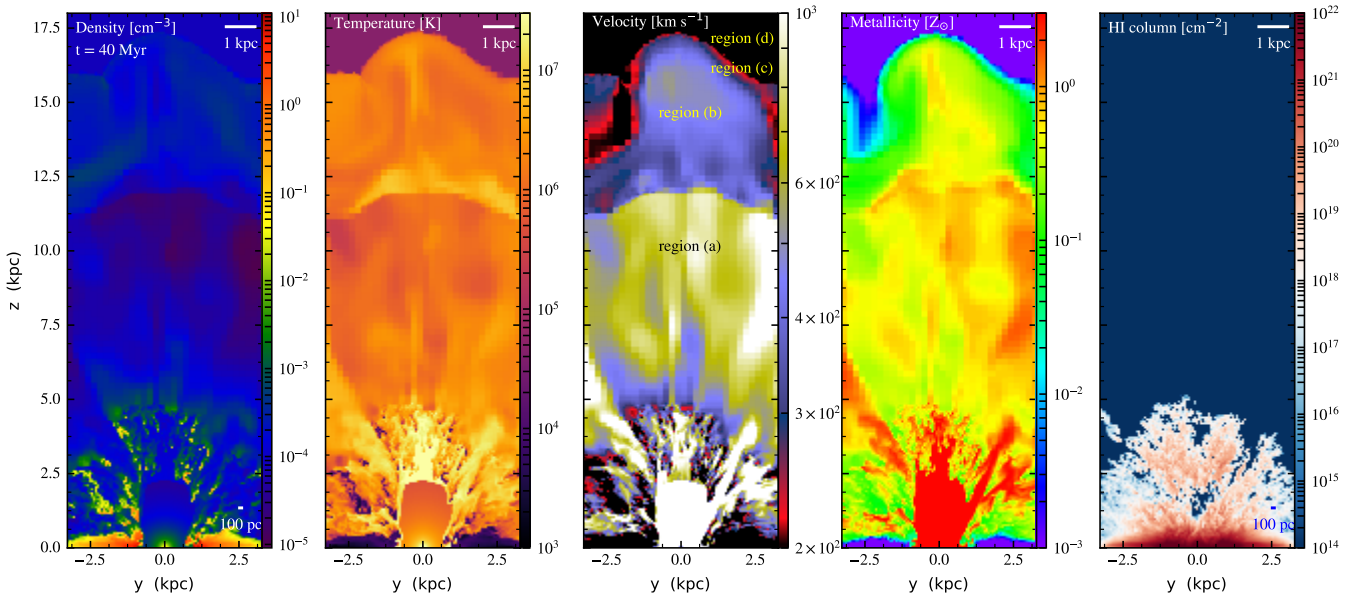


Figure 2. Sliced density, temperature, velocity magnitude, and metallicity (*from left to right*) distributions and a projected hydrogen column density distribution along the x-axis (*rightmost*) of the SNII-driven outflow at the box center (y-z plane) when the last SNII goes off at t=40 Myr. The middle figure denotes region a) expanding SNII enriched gas, b) shocked SNII enriched gas, c) swept-up CGM, and d) the ambient CGM.

The sliced density distribution in the y-z plane at $x = +1.42$ kpc from the disk center at $t = 160$ Myr (*left* in Figure 3) shows the formation of such fragments in the form of clumps and filaments. They are also visible as clumps and filaments in a projected distribution of neutral hydrogen along the x-axis at $t = 160$ Myr (*left* in Figure 4). These clumps and filaments will potentially produce weak MgII absorbers (we discuss our ion analysis in the next section). We call this process *phase 1* formation. They are made of SNII enriched outflow gas and their metallicity is ~ 0.1–$0.2 Z_\odot$. The size of clumps and the thickness of filaments are ∼100 pc. This size may be limited by our numerical resolution of 12.8 pc (Fujita et al. 2009; Gronke & Oh 2018). We discuss the effects of resolution further in Sec. 5.

Shortly after $t = 160$ Myr, a superbubble created by repeated SNIa explosions blows out of the dense ISM and SNIa enriched gas regains a tunnel for expansion, forming a SNIa driven outflow traveling at $v \sim 400$–500 km s^{-1}. In the projected distribution of neutral hydrogen at $t = 200$ Myr (*middle* panel in Fig. 4), fragments of swept-up ISM after blowout are visible framing a tunnel for outflow, and hot, low-density SNIa enriched gas in the outflow is seen as a cavity with $N_{HI} \lesssim 10^{13}$ cm^{-2} (we define SNIa enriched gas as region Ia).

By $t = 220$ Myr, this SNIa driven outflow (region Ia) expands into the cooled SNII enriched gas and the clumps and filaments of shocked SNII enriched gas (region b), shocking and sweeping them and forming more clumps and filaments. Figure 3 shows such a process clearly in a selected region at $z > 10$ kpc. These are potential candidates for weak MgII absorbers, too: we call this process *phase 2* formation. Their metallicity and size are likewise ~ 0.1–$0.2 Z_\odot$ and ∼100 pc. Hotter and lower-density shocked SNII enriched gas carries more metals ($Z \sim 0.4$–$1 Z_\odot$) and lies above $z \sim 14$ kpc.

The SNIa driven outflow continues to shock and sweep gas as well as clumps and filaments to the sides, and by $t \sim 300$ Myr, all the clumps and filaments as well as 58% of SNII outflow gas and 8% of SNIa outflow gas have left the box. Then, there is only very low-density gas with $n_H < 10^{-4}$ cm^{-3} left above the disk in the box. The metallicity of SNIa enriched gas is $Z \ll 0.1 Z_\odot$ as the metal production rate is about two orders of magnitude smaller than that of SNII, so it is still too early for any significant enrichment by SNIa. We stopped computing at $t \sim 450$ Myr.

With a realistic star formation history with multiple star clusters scattered in time and place, we expect *phase 1* and *phase 2* formation to be repeated in time and place to produce more clumps and filaments. We will test this scenario in a larger simulation box in our next paper.

4. WEAK MGII ABSORBERS AND CIV/OVI ABSORBERS

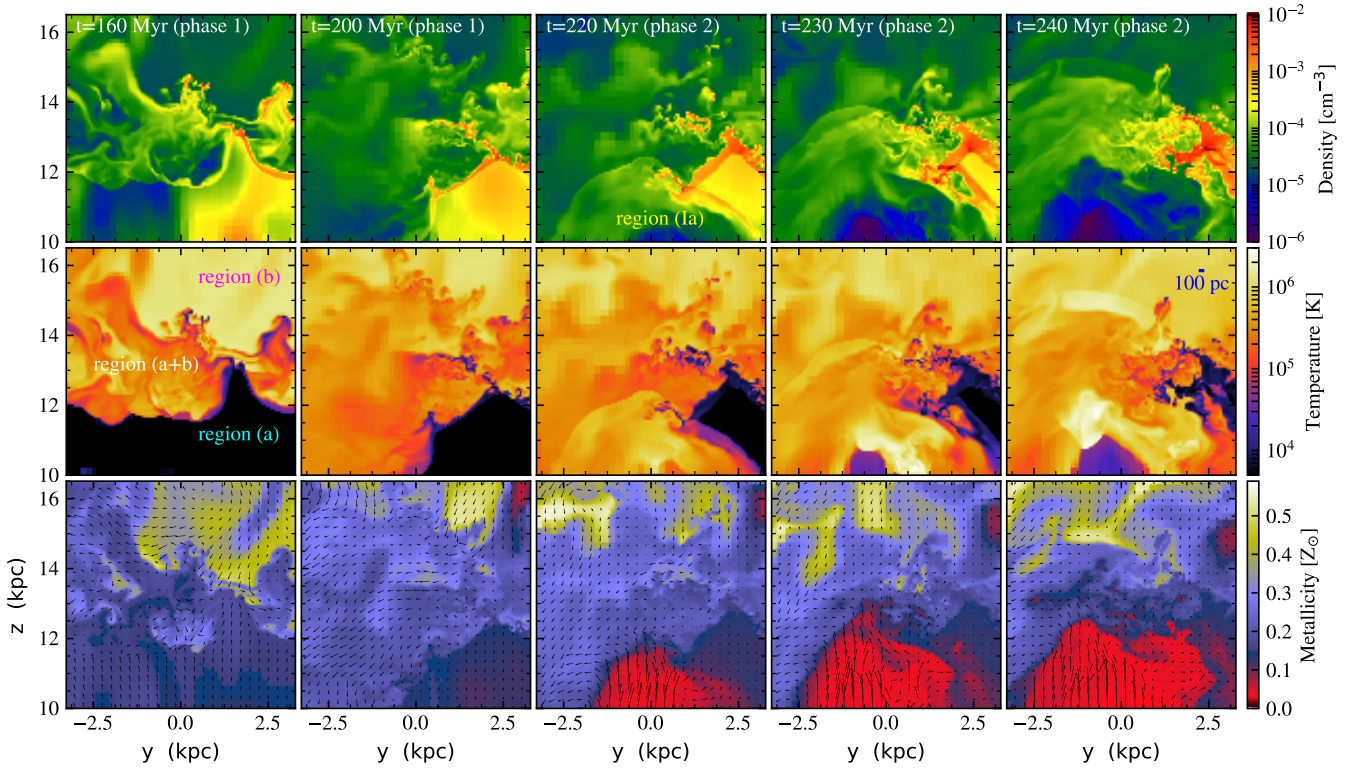


Figure 3. Sliced density (*top*), temperature (*middle*), and metallicity (*bottom*) distributions of cool, dense clouds at $x = +1.42$ kpc from the disk center in *y-z* plane at *phase 1* (t=160 and 200 Myr) and *phase 2* (t = 220, 230, and 240 Myr) *from left to right*. *Phase 1* formation begins when descending shocked SNII enriched gas (*region b*) collides with the expanding SNII enriched gas (*region a*) at the inner shock front, and *phase 2* formation begins when SNIa driven outflow (*region Ia*) rams into the rest of the SNII enriched gas and the clouds made at *phase 1*. The arrows in *bottom* figures show the direction of gas flow with $v_{max} = 429$ km s^{-1}.

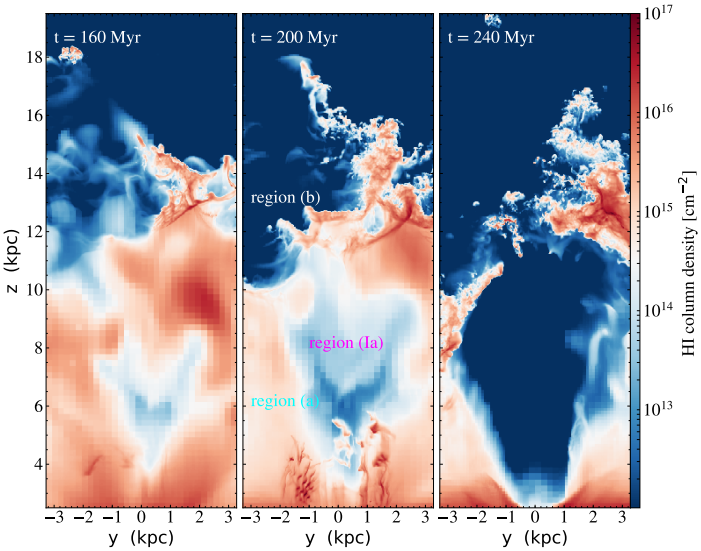


Figure 4. Projected neutral hydrogen distributions at t = 160 (*left*), 200 (*middle*), and 240 Myr (*right*), along the *x*-axis in the *y-z* plane. SNIa driven outflow is visible as a cavity (*region Ia*)

We calculate the fractions of HI, HII, MgII, CIV, and OVI ions using Trident as described in Section 2.4 by assuming all the gas in our simulation to be in photoionization equilibrium (PIE) with the UVB radiation at a given redshift (Haardt & Madau 2012). Our simulation does not include the effects of UVB radiation, so for example, expanding SNII enriched gas tends to overcool to lower temperature, $\lesssim 10^4$ K. However, this overcooled, low-density ($\leq 10^{-4}$ cm^{-3}) gas contributes very little to the total ion budgets, and denser clouds that produce MgII absorbers are self-shielded to the surrounding UVB radiation as long as $n_H \sim 5 \times 10^{-3}$ cm^{-3} at z=2 (Rahmati et al. 2013). Thus overcooling will not significantly affect our analysis (see Appendix).

4.1. *Overview*

Figure 5 shows projected density distributions of MgII, CVI, and OVI ions along the x-axis in the y-z plane at t=160, 200, and 240 Myr, and Figure 6 shows sliced density, temperature, metallicity, MgII, CVI, and OVI ion density distributions at x=+1.92 kpc from the disk center in the y-z plane at t=200 Myr. This sight line was

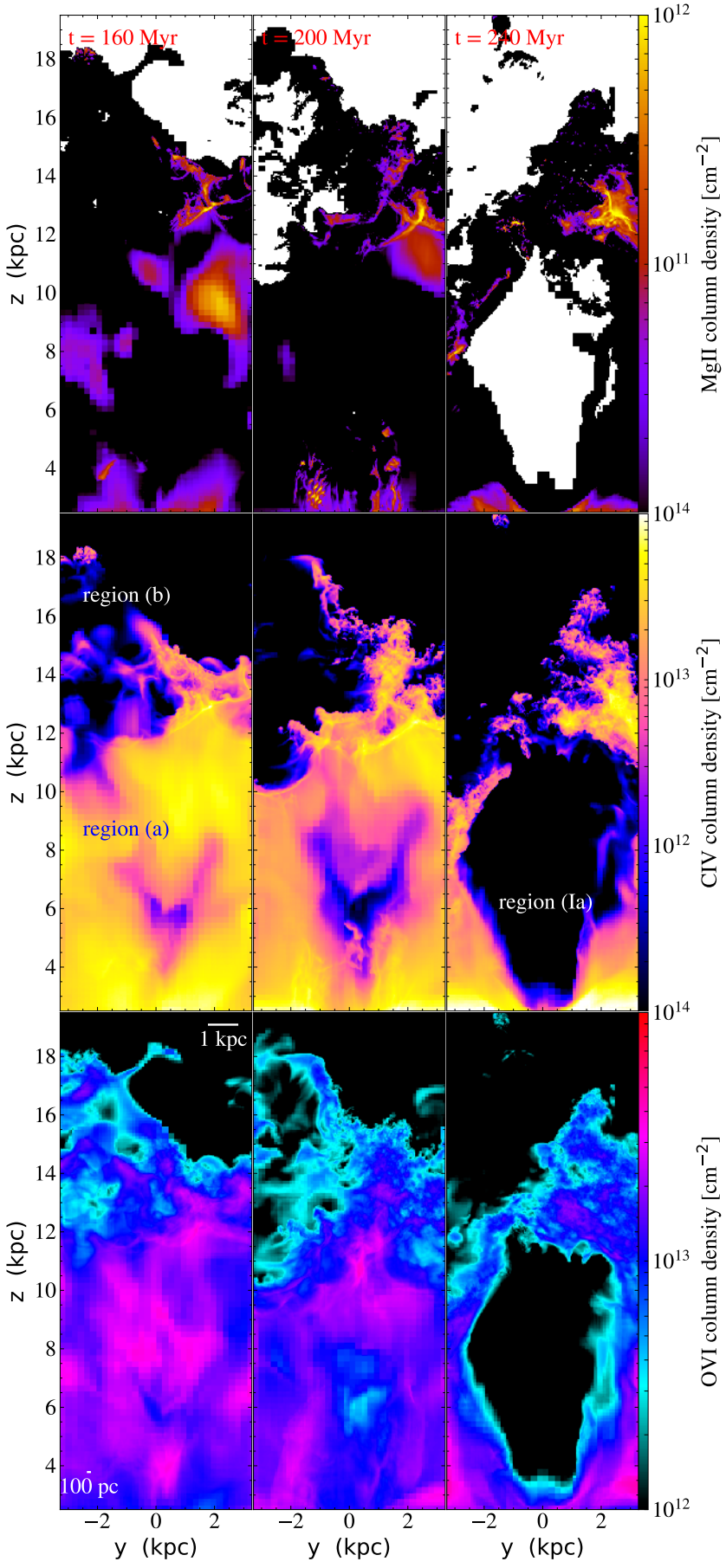


Figure 5. Projected MgII (*top*), CIV (*middle*), and OVI density (*bottom*) distributions at t = 160 (*left*), 200 (*middle*), and 240 Myr (*right*), along the x-axis in the y-z plane.

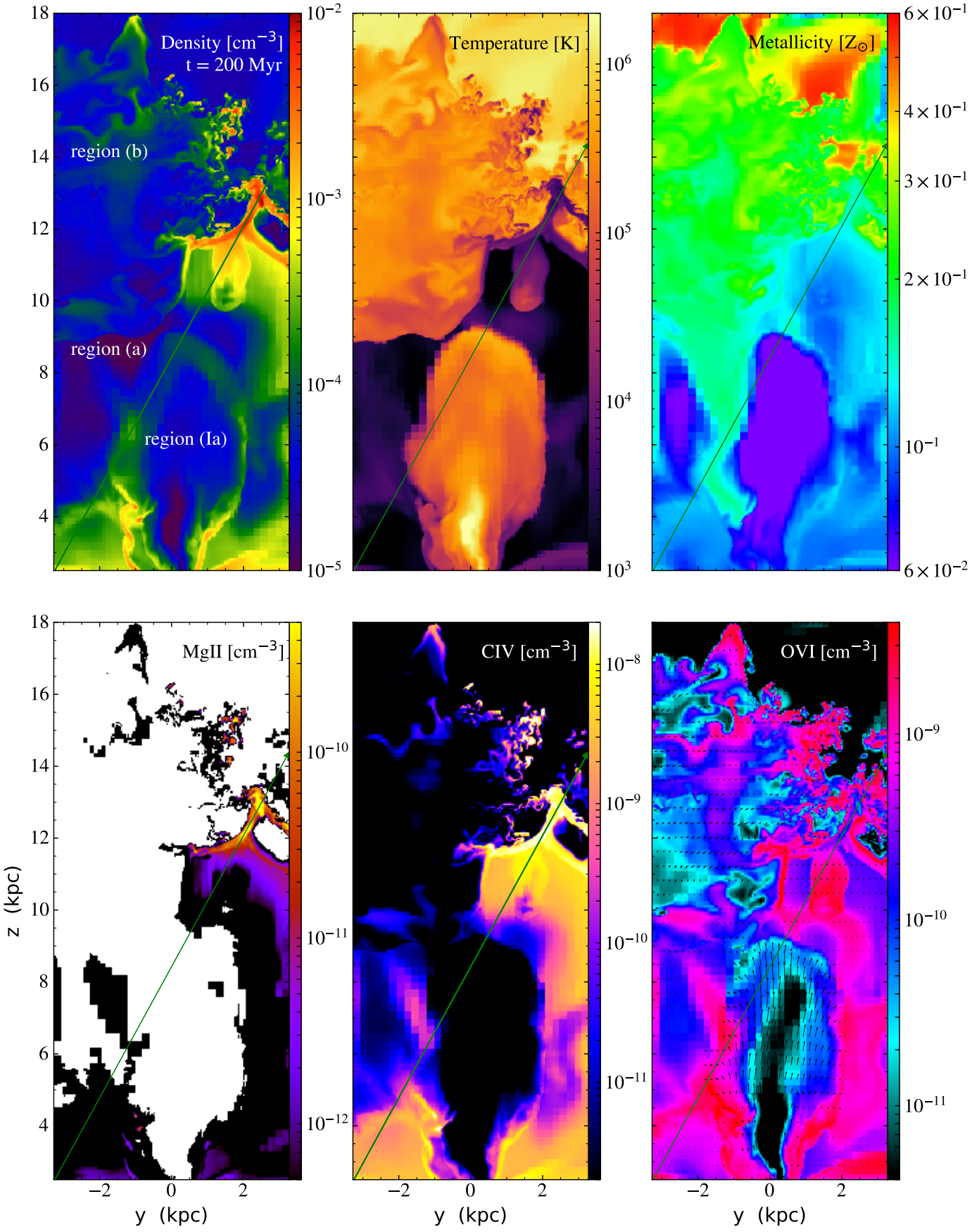


Figure 6. Sliced density, temperature, metallicity (*top from left to right*), and MgII, CIV, and OVI (*bottom from left to right*) density distributions at x=+1.92 kpc from the disk center in the y-z plane, at t=200 Myr. A line of sight from [x,y,z]=[+1.92 kpc, -3.28 kpc, +2.45 kpc] to [+1.92 kpc, +3.28 kpc, +14.4 kpc] is shown by a *green* line . The arrows in the *bottom right* figure show the direction of the gas flow with v_{max}=353 km s^{-1}.

selected as an example with a large pathlength through low ionization gas.

The clumps and filaments have hydrogen number densities, $n_H = 10^{-3}$ to 10^{-2} cm^{-3}, and their sizes/thickness, ∼100 pc, which is the smallest scale our simulation can resolve, as discussed in Section 3. Individual weak MgII absorbers seem to survive for ∼ 60 Myr, before they are mixed and diluted with the surrounding, warmer, lower-density gas, but they are continuously produced through *phase 1* to *phase 2* formation for over 150 Myr from a single instantaneous starburst source. Weak MgII absorption with $N_{MgII} > 10^{11}$ cm^{-2} is also found in a blob of gas that carries a swept-up ISM shell fragment in the expanding SNII enriched gas seen at e.g. [y,z]=[+2 kpc, 10 kpc] (see *top left* figure in Figure 5) and in fragmented shells of ISM swept-up by the SNIa driven outflow at e.g. z=2–4 kpc (see *top middle* figure in Figure 5). The blob has cooled slowly without fragmentation, and its size is $\gtrsim$ kpc. It is expanding into the *phase 1* shells in region (b) above, but SNIa driven outflow will shock and sweep up expanding SNII enriched gas including the blob in region (a) and the *phase 1* shells in region (b) to produce *phase 2* shells and fragments (see *top right* figure in Figure 5).

Higher ion absorbers are found in region (a) where expanding SNII enriched gas cools and in region (b) where shocked SNII enriched gas cools in *phase 1* and *phase 2*. In both cases, the hydrogen number density of the absorbers is n_H ∼a few $\times 10^{-4}$ cm^{-3}, but the absorbers in region (a) extend over 1-4 kpc while the absorbers in region (b) are smaller, 500 pc–1 kpc. The sizes of high ion absorbers agree with the observed estimates for CIV absorbers by Misawa et al. (2008) and Schaye et al. (2007). They are ∼100 pc - 5 kpc in a sub-LLS ($10^{14.5} < N_{HI} < 10^{16}$ cm^{-2}) or Lyα forest environment ($N_{HI} < 10^{14.5}$ cm^{-2}). CIV absorbers in region (b) are clumpy and filamentary and some surround weak MgII absorbers, so both of them arise from the same clumps and filaments created in *phase 1* and *phase 2* formation. However, CIV ions in these clumps and filaments survive longer than MgII ions by another 20-30 Myr. Our simulations suggest clouds that produce MgII absorbers also produce CIV absorbers, and MgII absorbers probe the densest parts of the clouds while CIV absorbers extend out to more diffuse, larger regions. In the process of mixing, the regions that produce MgII absorption disappear first due to dilution, so our simulations agree with a picture proposed by Schaye et al. (2007) that expanding MgII absorbers with high metallicity ($Z \lesssim Z_\odot$) produce CIV absorbers.

OVI absorbers in region (b) appear even more diffuse, arising in larger ($\gtrsim$ 1 kpc) clouds, that are not necessarily the same clouds that host MgII and CIV clouds nor in the same phase. On the other hand, most OVI absorbers in region (a) arise from the same clouds that host CIV absorbers in the same phase.

We find that 1-3% of high ions by mass are from collisional ionization, and they are found in coronal OVI absorbers in region (b). This is consistent with observational analyses that photoionization dominates in sub-LLS and Lyα forest environments at intermediate to high redshift. (e.g. Simcoe et al. 2004; Schaye et al. 2007; Lehner et al. 2016).

Figure 7 shows physical values along a line of sight through the simulation box, which is noted in *green* in Figure 6, and Figure 8 shows mock spectra created along the sightline with Trident. Along the sightline, there are two MgII absorbers which correspond to two peaks in Figure 6 and in the *bottom left* plot of Figure 7. They are shocked cooling shells in region (b) and are only separated by a small velocity in the spectrum, despite their spatial separation (Δv∼2 km s^{-1} at v∼38 km s^{-1}), which is visible in the absorption profile as a slight asymmetry(Figure 8).

The same shells produce CIV absorption, but no OVI absopbtion. OVI absorbers in region (b) are in a different, coronal phase. CIV absorbers in region (a) are > few kpc in size: one is at z∼2.5 kpc with a positive velocity (v∼10 km s^{-1}), one is at z∼2.5-4 kpc with a nagative velocity (v∼-5 km s^{-1}), one is at z∼10–11 kpc (cooler, v∼30 km s^{-1}) and the other is at z∼11–12 kpc (warmer, v∼40 km s^{-1}), both below the cooling shell (v∼38 km s^{-1}). The first two absorbers produce the double absorption profiles in Figure 8, and the last two absorbers produce the saturated absorption profile at v=20–45 km s^{-1}, together with CIV absorbers in region (b).

OVI absorbers in region (a) arise from the same cold clouds, producing two sets of double absorption profiles, but the sightline is also going through a turbulent mixing layervof swept-up shells by the SNIa driven outflow at z=5–7 kpc. Its temperature is $\gtrsim 10^5$ K. The signal is buried in the double absorption profiles at v∼10 km s^{-1}. The OVI absorber in region (b) is coronal and turbulent with v∼-10–40 km s^{-1}, but is weak compared with the other OVI absorbers.

We note that some SNII outflow gas in region a cools to temperature below 10^4 K by t$\gtrsim$200 Myr, however, this overcooled, low-density ($\leq 10^{-4}$ cm^{-3}) gas only makes a little contribution to CIV and OVI column column densities (see Appendix).

Figure 8 also shows that our mock spectra reproduce qualitative features of the observed profiles of observed

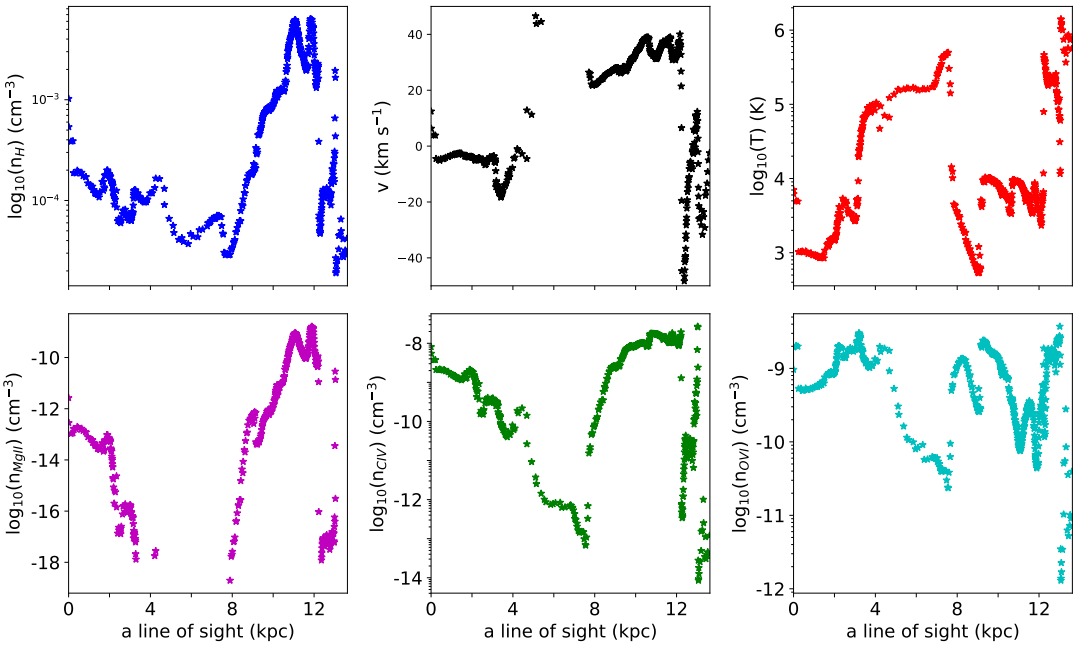


Figure 7. Hydrogen density (*top left*), sightline velocity (*top middle*), temperature (*rop right*), MgII density (*bottom left*), CIV density (*bottom middle*), and OVI density (*bottom right*) distributions along the line of sight from [x,y,z]=[+1.92 kpc, 0 kpc, 2.45 kpc] to [+1.92 kpc, 6.55 kpc, 14.4 kpc] (*green line* in Figure 6) at t=200 Myr.

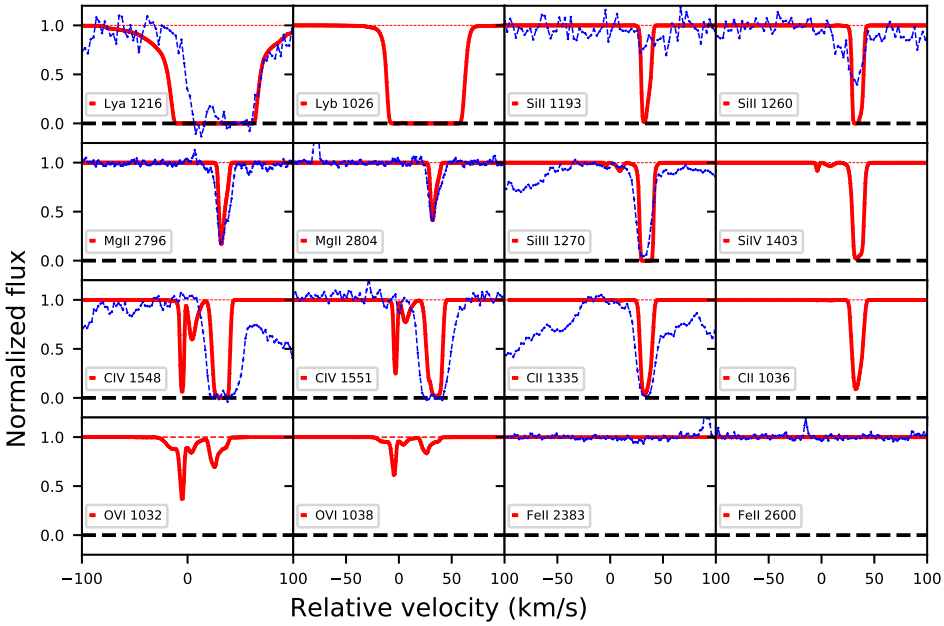


Figure 8. Mock spectra along the line of sight (*green line* in Figure 6) at t=200 Myr, compared to the observed profiles of system 3 at z=1.75570 (*blue dashed line*, Misawa et al. 2008).

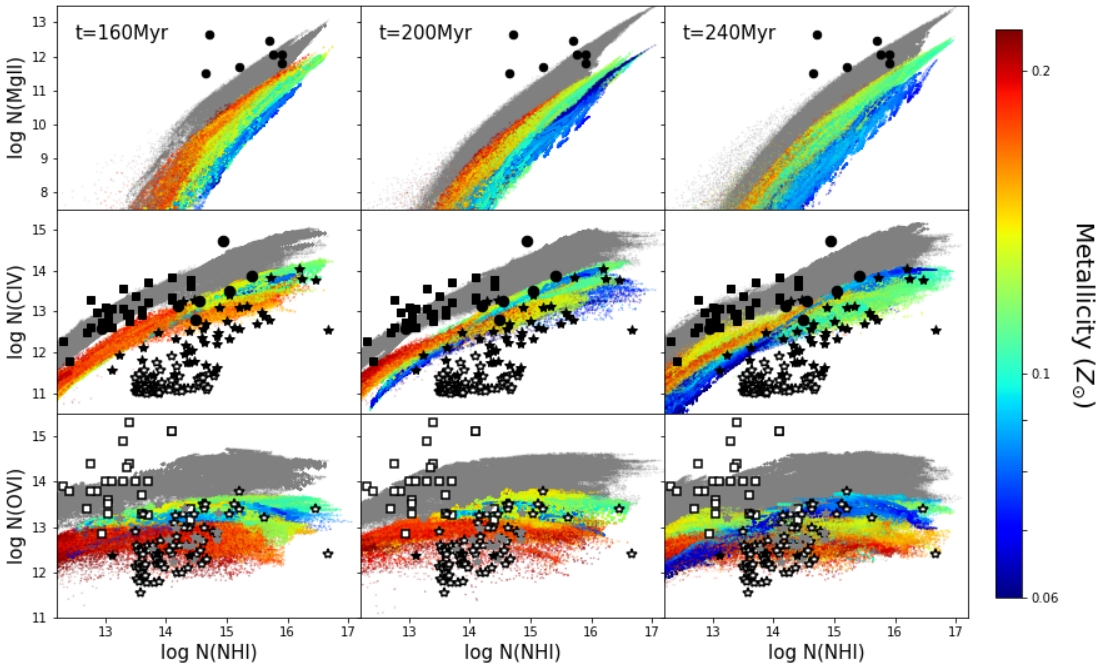


Figure 9. MgII (*top row*), CIV (*middle row*), and OVI (*bottom row*) versus HI column densities in sightlines parallel to each of the three cardinal axes at t=160 (*left column*), 200 (*middle column*), and 240 Myr (*right column*) with different colors indicating MgII, CIV, and OVI density-weighted metallicities, to be compared to the observed MgII/CIV clouds by Misawa et al. 2008 (*circle*) and the observed CIV/OVI observations by Schaye et al. 2007 (*square*) and D'Odorico et al. 2016 (*star, but gray star for detection of only one member of the doublet*) . Note OVI densities from Schaye et al. 2007 (*open square*) and CIV and OVI densities from D'Odorico et al. 2016 (*open star*) are upper limits (*open square*). Grey points indicate ion versus HI column density distributions expected when all the gas in our simulation is assumed to have solar metallicity.

weak MgII system 3 at z=1.75570 published in Misawa et al. (2008).

4.2. *Comparison to observations*

4.2.1. *Column densities and metallicities*

In Figure 9, we show the relations between ion column densities and HI column densities in our simulation at t=160, 200, and 240 Myr in sightlines parallel to each of the three cardinal axes, and compare them with the observed relations. The colors indicate MgII, CIV, and OVI density weighted metallicities respectively. Effective lower limits to the MgII, CIV, and OVI column densities are 3.5×10^8, 7.5×10^8, and 4.7×10^9 cm^{-2} in our simulations. MgII, CIV, and OVI absorbers in our simulation are enriched to Z=0.1-0.2 Z$_\odot$ by SNII from an instantaneous starburst, as the SNIa contribution is negligible at this point.

Top figures in Figure 9 show that sightlines with higher metallicities have higher MgII column densities at given HI column densities, and they are compared to the MgII-HI observations from three MgII absorbers at z$\sim$ 1.7 from Misawa et al. (2008) and four MgII absorbers at lower redshift (z=0.65-0.91) from Charlton et al. (2003) and Ding et al. (2005). The MgII column densities in our simulation are up to 1 order of magnitude smaller than the observed values at the given HI column densities, $N_{HI} > 10^{15}$ cm^{-2} (i.e. sub-LLS). This is mainly because our simulation can only be run up to $\sim$ 300 Myr before most gas leaves the grid: metal mixing and cooling should be computed for a much longer duration, also including the SNIa metal contribution. More-

over, we set the initial metallicity of our dwarf disk and halo gas to be Z=10^{-3} $Z_{\odot}$, to study the effects of metal contribution by our simulated starburst alone. Thus, we are likely underestimating the metallicities of MgII absorbers. If we assume that all the gas in our simulation box has a solar metallicity, the boosted MgII column densities (*grey* points in Figure 9) agree more with the observed values.

At lower $N_{HI} < 10^{15}$ cm^{-2}(i.e. sub-LLS to Lyα forest), there is no dense cloud formation in our simulation thus no MgII clouds with $N_{MgII} > 10^{11}$ cm^{-2}. There are two MgII absorbers with $N_{HI} < 10^{14.5}$ cm^{-2} at z$\sim$2 (Misawa et al. 2008) and their MgII column densities are larger than predicted by our simulations for sightlines with this N_{HI} by two orders of magnitude. This might also be due to lower metal enrichment in our simulation. The estimated metallicities for the two absorbers are very high, Z=0.63-0.79 and even super solar, Z$>$ 7.9 $Z_{\odot}$ respectively. This discrepancy could also be related to the limited simulation resolution. We hope to study the possible formation of super solar, weak MgII clouds with our future global simulations.

Simulated CIV column density distributions appear to agree better with the observed column densities of CIV absorbers that are found in the same sightlines with the MgII absorbers studied by Misawa et al. (2008). These CIV absorbers are in sub-LLS environments, and have similar metallicities, Z=0.1-0.3 $Z_{\odot}$ to our simulation values, except for one absorber with Z=0.8 $Z_{\odot}$: this metal rich CIV absorber is in a structure related to the super solar, weak MgII absorber with Z$>$ 7.9 $Z_{\odot}$.

On the other hand, our simulated CIV column densities are smaller than those of the CIV absorbers studied by Schaye et al. (2007): the disagreement is by an order of magnitude. This is probably because these absorbers are selected for the high metallicities, Z$\sim$ $Z_{\odot}$. They are found in Lyα forest environments and are smaller in size ($\sim$500 pc – 1 kpc). In our simulation, smaller CIV clouds are found in region (b) and arise from the same clouds that currently host or used to host even smaller, weak MgII absorbers in sub-LLS to Lyα forest environments. Our metallicity boosted values better agree with the observations (Figure 9). The upper limits for OVI column densities associated with the observed CIV absorbers (Schaye et al. 2007) are also above what our simulation predicts, and lie in the metallicity boosted grey area, just like most of the observed weak MgII and CIV absorbers. There is no other information about their physical properties available.

The observed CIV column densities by D'Odorico et al. (2016) appear to agree with our simulated values at $N_{HI} > 10^{14.5}$ cm^{-2}, however, they are much lower than our simulated values, by up to one order of magnitude, at $N_{HI} < 10^{14.5}$ cm^{-2}. These CIV absorbers are observed at a higher redshift, z$\sim$ 2.8, and the majority of them have their estimated metallicities between $10^{-2.5}$ $Z_{\odot}$ and 10^{-2} $Z_{\odot}$, much lower than our simulated values. There is no information about the physical properties available for the CIV and OVI absorbers observed by D'Odorico et al. (2016). The data for OVI column densities are mostly upper limits except three detections of which one shows a very weak CIV line and another shows none. Out of 15 OVI possible detections with single lines, six of them do not show an associated CIV line. Despite the estimated low metal contents, the observed OVI column densities and their upper limits appear to agree better with our simulated values at all HI environments. The sizes and thermal properties are unknown for these CIV and OVI absorbers.

We note that the observed estimates and upper limits for CIV and OVI column densities at given HI column densities vary over 4 orders of magnitudes. This may be due to the presence of HI dominated gas in observed sightlines which originate in regions that are not covered by our simulations. However, for MgII absorbes and associated CIV absorbers, a major reason for the discrepancy seems to be a lack of metal enrichment as well as the low initial metallicity of disk and halo gas in our simulation. We speculate that galactic outflows from repeated bursts of star formation for a longer duration ($\sim$ 1 Gyr) will eventually create high-metallicity, complex structures of multiphase gas.

4.2.2. *Covering fractions*

Figure 10 shows fractions of sight lines that occupy our simulation box above the galactic disk and within the virial radius as functions of MgII, CIV, and OVI column densities along x, y, an z axes at three different times. The *Grey* region in Figure 10 depicts predicted fractions of sight lines as a function of column densities of the observed weak MgII absorbers at various redshifts by Rigby et al. (2002); Charlton et al. (2003); Ding et al. (2005); Misawa et al. (2008); Narayanan et al. (2008), based on an assumption that they cover $\sim 5-30\%$ of a halo. The total covering fraction of weak MgII absorbers in L* galactic haloes is estimated to be $\sim$ 30% by Narayanan et al. (2008); Muzahid et al. (2017). If a sightline goes through N dwarf satellite galaxies, the covering fraction in each dwarf halo would need to be approximately 0.3/N. We would need a similar fraction of dwarf satellite haloes to be covered with weak MgII absorbers, if undetected, satellite dwarf galaxies are responsible for producing weak MgII absorbers in a L* halo.

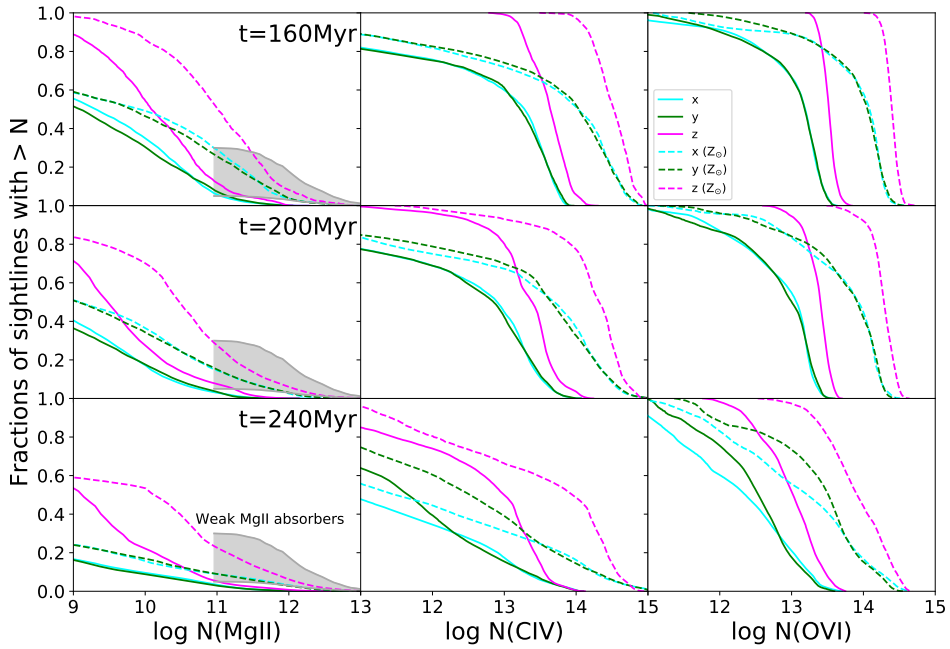


Figure 10. The MgII (*left*), CIV (*middle*), and OVI (*right*) covering fractions as functions of column densities along each of the three cardinal axes at t=160 (*top*), 200 (*middle*) and 240 Myr (*right*). All sightlines between z=2.5 kpc (the disk edge) and 17.5 kpc (virial radius) are included. The *dasremote.net.ed.ac.ukhed lines* show the covering fractions when all the gas is assumed to have solar metallicities. The *grey region* indicates estimated fractions of sight lines as a function of MgII column densities when we assume that the observed weak MgII clouds at various redshifts (Rigby et al. 2002; Charlton et al. 2003; Ding et al. 2005; Misawa et al. 2008; Narayanan et al. 2008) cover 5–30% of a halo. The observed MgII column densities are $\geq 10^{11}$ cm^{-2}.

Weak MgII absorbers with column densities greater than the observed minimum, $\sim 10^{11}$ cm^{-2} occupy about only $f_{MgII} \sim 5\%$ of the dwarf halo in our simulation. However, this is a lower limit for the covering fraction because $38 - 58\%$ of SNII outflow gas leaves the box by $t = 40 - 300$ Myr. Boosting the metallicities of all the gas to 1 $Z_\odot$ (see *dashed* lines in Figure 10) raises the fractions of sight lines with $N_{MgII} \gtrsim 10^{11}$ cm^{-2} to $f_{MgII} \sim 30\%$, but there is still a deficiency of MgII clouds with higher column densities, $\gtrsim 10^{12}$ cm^{-2}. Most observed weak MgII absorbers have column densities $\gtrsim 10^{12}$ cm^{-2}. As we argued in the previous section, repeated bursts of star formation will likely create more clumps and filaments, like the brightest structures in Figure 5, through cycles of *phase 1* and *phase 2* formation. Then, a larger fraction of the dwarf galaxy halo may be covered with moderately dense MgII absorbers. However, the formation of denser, high column density, weak MgII clouds may require other mechanisms that involve more gas and more metals with stronger shocks, as the shell density scales like the square of the Mach number in the isothermal shocks expected, so more powerful outflows may be responsible for the higher column density MgII absorbers. In addition, interaction of outflows with cosmological infall will likely produce stronger shocks, so possibly denser clouds. Note we have a static background in our simulations. However, cooling is strongly limited by numerical resolution, so gas behind isothermal shocks will not cool to the theoretical density (nM^2) even with 0.2 pc resolution Fujita et al. (2009).

We can estimate the number density of weak MgII absorbers per unit comoving path length to be $dN_{MgII}/dX \approx 0.21$ assuming $f_{MgII} \sim 5\%$ for $N_{MgII} \geq 10^{12}$ cm^{-2} when metallicity is boosted to Z=$Z_\odot$, 1.13 Mpc^{-3} for halo comoving number density with $M_{halo} \geq 3 \times 10^9$ $M_\odot$ at z=2 (Murray et al. 2013), and $\pi(17.5^2 - 2.5^2)$ kpc^2 for halo proper cross section. This yields a value comparable to $dN_{MgII}/dX = 0.33$ at 1.4 <z< 2.4 found by Narayanan et al. (2008) and $dN_{MgII}/dX = 0.41$ at <z>=2.34 by Codoreanu et al. (2018). Likewise, the number density of high ionization clouds (CIV and OVI) per unit comoving path length is estimated to be $dN_{CIV}/dX \approx dN_{OVI}/dX \approx 2$ with $f_{CIV} = f_{OVI} \sim 50\%$. As a reference, it is $dN_{CIV}/dX \approx 9$ at z ~3 based on Figure 6 of D'Odorico et al. (2016), which includes all CIV systems along a line of sight, not necessarily only those confined to the CGM of galaxies. The covering fractions of CIV and OVI ions are measured to be 0.3-0.8 at impact parameters $\lesssim 1$ pMpc around star-forming galaxies at z~2.4 (Turner et al. 2014). It is interesting to note that the comoving MgII mass density

seems to increase nearly a factor of 10 from <z>=2.34 to <z>=4.77 (Codoreanu et al. 2018) with a large number of weak MgII absorbers even up to z∼7 (Bosman et al. 2017). This high incidence of MgII absorbers suggests that they are associated with dwarf galaxies, including smaller, numerous galaxies during the epoch of reionization, and the presence of the abundant weak MgII absorbers must be explained without more powerful outflows from larger galaxies.

We assess this as follows: 1) a SNII driven outflow is launched from a star cluster every 100 Myr, the time by which gas flows back to the central source region in our simulation, and it takes 50 Myr for a SNII driven outflow with v=200-400 km s^{-1} to reach the shocked enriched gas from previous outflows (region b). 2) SNIa drive a superbubble and an outflow after SNII stop in 50 Myr (we choose 50 instead of 40 Myr for simplicity), and it takes 100 Myr for a SNIa driven outflow to reach region (b) based on our simulation result. 3) repeated bursts last for 1 Gyr. 4) interaction from a newly launched outflow produces weak MgII absorbers that cover 3-6% of our dwarf halo and those weak MgII absorbers survive for at least 150 Myr based on our simulation result. Then, we estimate that the covering fraction of dwarf halos by weak MgII absorbers will be 12-24%. This number should go up once the CGM is more metal enriched, because the covering fraction of 3-6% is computed when metallicities of absorbers are Z=0.1-0.2 $Z_\odot$. We hope to test this hypothesis with our future global simulation in a larger box with repeated bursts in time and place.

5. RESOLUTION STUDY

Our *standard* simulation employs a highest resolution of 12.8 pc with four refinement levels, thus resolves ∼ 100 pc structures for our purposes. We base the estimate of roughly eight cells being required to minimally resolve structures on two arguments. First, the numerical dissipation range for supersonic turbulence computed with Enzo extends over almost an order of magnitude (e.g. Kritsuk et al. 2007, Figure 5), similar to most other grid codes (Kitsionas et al. 2009). Second, modeling of a cloud in a supersonic flow shows that a radius of six zones using a second-order method is insufficient to capture fragmentation by instabilities (Mac Low & Zahnle 1994, Figure 4).

To study the extent to which the production of clumps and filaments as well as their sub-structures and fragmentation are dependent on numerical resolution, we ran the same simulation with 3 refinement levels (*low-res* simulation), and by applying 5 refinement levels in a region where the largest filaments form at [Δx,Δy,Δz]=[(-0.5 kpc, 3.28 kpc), (-0.5 kpc, 3.28 kpc), (10 kpc, 15 kpc)] (*high-res zoom* simulation). We only ran the *high-res zoom* simulation up to t=200 Myr.

Figure 11 shows *phase 1* formation of filaments and clumps computed with the three different resolutions. Figure 11 compares the degrees of fragmentation in *high-res zoom* and our *standard* simulations. In the *high-res zoom* simulation, gas fragments into thinner filaments and smaller clouds compared with our *standard* simulation. The smallest structures are resolved across ∼8 cells, so they are ∼50 pc in the *high-res zoom* simulation compared with ∼100 pc in our *standard* simulation. These filaments and clumps will further fragment into smaller pieces with higher resolution. Gas structures seem drastically different in the *low-res* simulation, with much larger clouds compared with the higher resolution runs.

Despite the differences in fragmentation seen in simulations with different resolutions, there is no significant difference in projected MgII distributions (*bottom* figures). We see no change in the fraction of weak MgII absorbers with high column densities, and the covering fractions of weak MgII absorbers as well as CIV and OVI absorbers remain practically the same. We will add ion versus HI column density distributions with metallicities (Figure 13) and ion covering fractions as functions of column densities (Figure 14) for the *low-res* simulation in the appendix.

We conclude that resolution has a small effect on the projected distribution of dense clumps and filaments, and this in turn warns us to be very careful when we interpret observations (Peeples et al. 2019). There is a possibility that, at much higher resolution filaments and fragments will further "shatter" into ∼pc sized cloudlets that agree with some of the observed MgII absorbers (Gronke & Oh 2018; McCourt et al. 2018; Gronke & Oh 2020; Begelman 1990), but to test this possibility requires 1/10th pc resolution in a galactic-scale simulation which is not feasible at the moment. Opposing fragmentation is possible cloud coalescence, which may be numerically challenging to reproduce in 3D simulations (Waters & Proga 2019).

6. SUMMARY

In this paper, we use hydrodynamical simulations of galactic outflows to explore the production of weak MgII absorbers and CIV and OVI absorbers in the CGM of a dwarf satellite galaxy with a halo mass of 5×10^9 $M_\odot$ at $z = 2$, expected to be hosted by a larger L^* halo. With our standard numerical resolution of 12.8 pc, we model the formation of superbubbles and outflows from a galactic disk assuming a single instantaneous starburst in a simulation box with dimensions (6.5536, 6.5536,

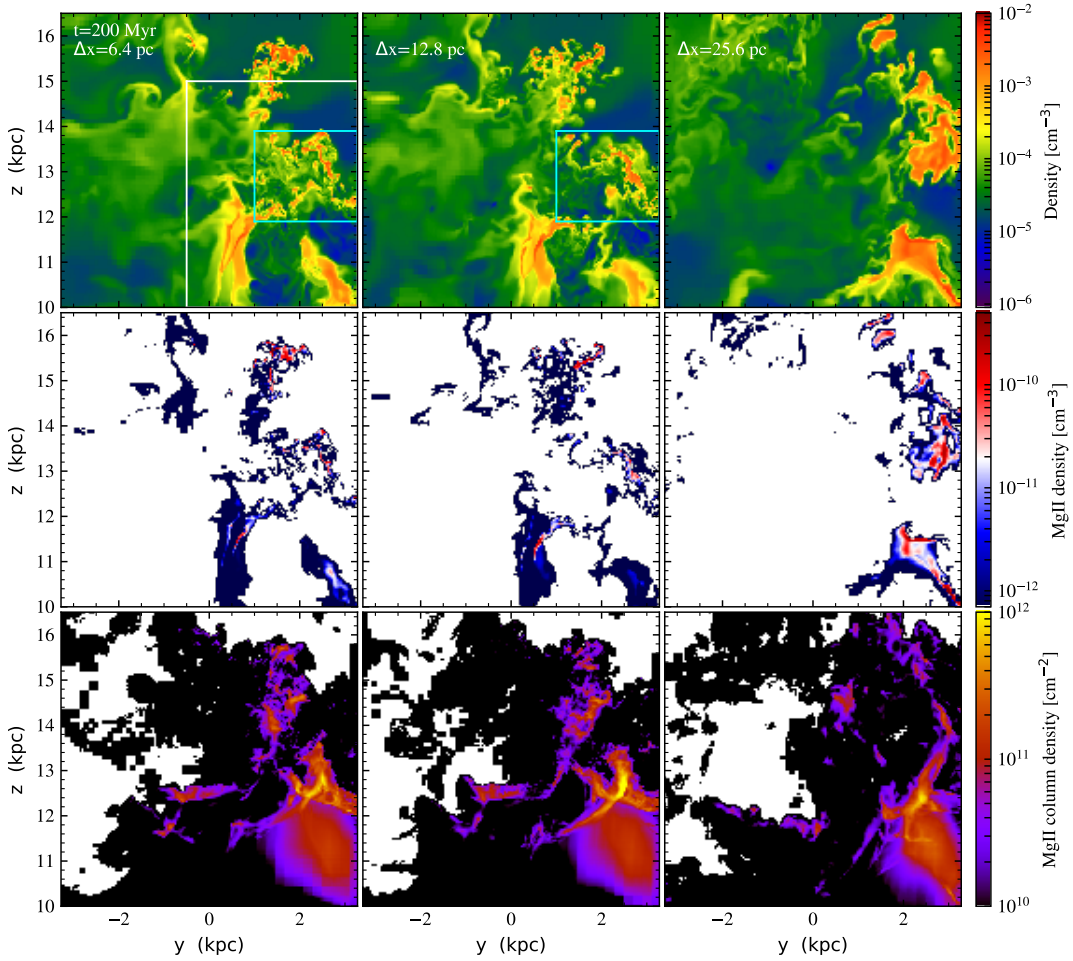


Figure 11. Sliced density (*top*) and MgII density (*middle*) distributions at x=+2.4 kpc from the disk center and projected MgII distributions (*bottom*) along the x-axis, all in the y-z plane, at *phase 1* (t=200 Myr), resolved with highest resolutions of 6.4 in [Δx,Δy,Δz]=[(-0.5 kpc, 3.28 kpc), (-0.5 kpc, 3.28 kpc), (10 kpc, 15 kpc)] (*white rectangle*), 12.8 (our *standard* simulation), and 25.6 pc (*from left to right*). Regions enclosed in *cyan* rectangles are shown in Figure 12.

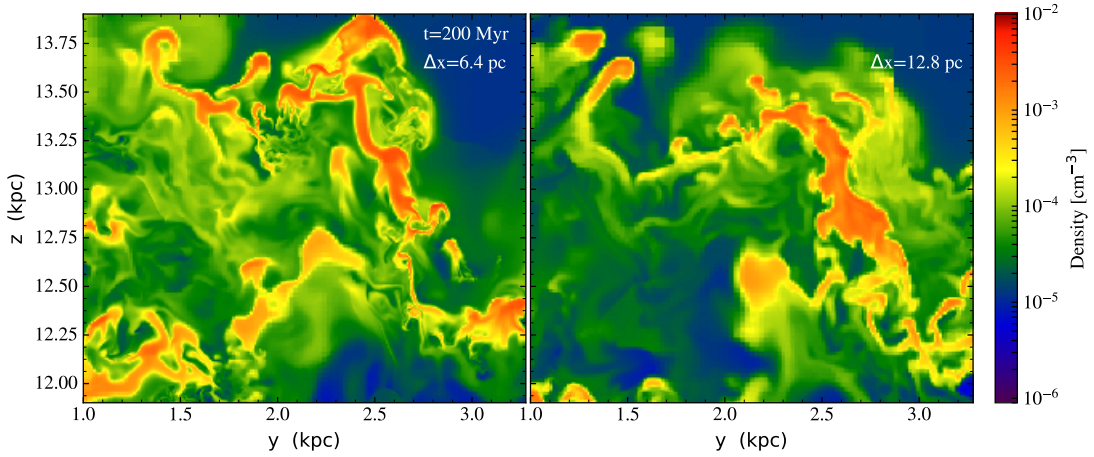


Figure 12. The same as *top* figures in Figure 11, but showing only regions enclosed in *cyan* rectangles for 6.4 (*left*) and 12.8 (*right*) resolutions.

32.768) kpc, and study the interaction and cooling of metal enriched outflowing gases. Although we ran the

simulations only for a duration of ∼300 Myr, as most metal enriched gas leaves the simulation box by this time, our results highlight the possibility of dwarf galactic outflows producing transient, but continuously generated MgII clouds as well as larger CIV and OVI clouds in sub-LLS and Lyα forest environments.

Our main findings are:

- Thin, filamentary, weak MgII absorbers are produced in two stages:
  - *phase 1* shocked SNII enriched gas loses energy and descends toward expanding SNII enriched gas and is shocked, cools, and fragments.
  - *phase 2* SNIa driven outflow gas shocks the SNII enriched gas as well as *phase 1* shells, which then cool and fragment.

  The width of the filaments and fragments are $\lesssim$ 100 pc with our standard numerical resolution. A single MgII cloud survives for $\sim$ 60 Myr, but we suggest MgII absorbers will continuously be produced through cycles of *phase 1* and *phase 2* formation for $>$ 150 Myr by repeated bursts of star formation.

- CIV absorbers are produced in expanding SNII enriched gas (region a) and shocked SNII enriched gas (region b). CIV absobers in region (a) extend over 1–4 kpc and CIV absorbers in region (b) are smaller, 500 pc–1 kpc, but they are both cool and photoionized. The smaller CIV absorbers originate from the same clouds that produce weak MgII absorbers, and they surround the dense MgII clouds. As the clouds get destroyed and mixed with the surrounding gas, MgII absorbers disappear first, but CIV absorbers survive for another 20–30 Myr.

- OVI absobers are also produced in expanding SNII enriched gas in region (a) and shocked SNII enriched gas in region (b). OVI absorbers in region (a) originate from the same cool clouds that produce CIV absorbers, but OVI absorbers in region (b) are not coincident with MgII absorbers or CIV absorbers. Their sizes are over $\gtrsim$1 kpc.

- CIV absorbers and most OVI absorbers are cool, photoionized clouds while OVI absorbers arising in turbulent mixing layers in region (b) are hotter and collisionally ionized. Photoinization dominates in sub-LLS and Lyα environments at intermediate redshft .

- The metallicities of MgII, CIV, and OVI absorbers are Z=0.1–0.2 Z$\odot$ by t=$\sim$200–300 Myr, with only one cycle of *phase 1* and *phase 2* formation in a dwarf disk and halo with a low initial metallicity, Z=0.001 Z$\odot$. We speculate that the clouds forming in shocked outflow gas (region b) will be progressively enriched with more metals when bursts of star formation are repeated.

- A lower limit for the covering fraction of weak MgII absorbers in our dwarf halo is 3–6% because we compute only one cycle of *phase 1* and *phase 2* formation and more than half the metal enriched gas leaves the simulation box early. To reproduce the observed estimate for the covering fraction in a L* halo (30%) with outflows from such galaxies alone, sightlines must go through haloes of multiple dwarf satellite galaxies. We also speculate that the covering fraction in a single dwarf halo will be boosted with repeated bursts with many cycles of *phase 1* and *phase 2* formation in a large simulation box that covers the entire halo.

There are two major problems in our current simulations: 1) a deficiency of weak MgII absorbers with high column density, $\gtrsim 10^{12}$ cm^{-2} and 2) low metallicity of weak MgII absorbers.

1) The formation of denser, high column, weak MgII absorbers may require stronger shocks with more powerful outflows and/or outflows interacting with dynamic infall. Repeated outflows shocking the clumps and filaments formed by previous outflows may also produce denser MgII clouds. However, cooling behind shocks is limited by numerical resolution. Our resolution study shows that the sizes of filaments and fragments decrease by a factor of two with a resolution twice as high, however, the projected properties are insensitive to changes in resolution that is $\gg$ pc. We may need less than a pc scale resolution to address this problem.

2) The metallicity, less than solar, of our MgII absorbers is the result of our assumption of a single instantaneous starburst and the limited duration of our simulations ($\sim$ 300 Myr) neglecting the SNIa metal contribution. Starting with a higher initial metallicity for our dwarf disk and halo gas will also alleviate the problem.

This paper nonetheless highlights the possibility of galactic outflows from invisible, dwarf satellite galaxies to produce highly enriched, multiphase gas. We hope to address the remaining problems with our next, more global simulations.

ACKNOWLEDGMENTS

This work was supported by the Grants-in-Aid for Basic Research by the Ministry of Education, Science and Culture of Japan, Grant Number 19K03911. We acknowledge use of the Cray XC50 at the Center for Computational Astrophysics (CfCA) of the National Astronomical Observatory of Japan (NAOJ). J.C.C. acknowledges support by the National Science Foundation under grant No. AST-1517816. AM acknowledges support from UK Science and Technology Facilities Council, Consolidated Grant ST/R000972/1. M-MML was partly supported by US NSF grant AST18-15461. Computations described in this work were performed using the publicly available `Enzo` code (http://enzo-project.org), which is the product of a collaborative effort of many independent scientists from numerous institutions around the world. Their commitment to open science has helped make this work possible.

Facilities: CfCA(NAOJ)

Software: Enzo (Bryan et al. 2014), yt (Turk et al. 2011) Trident (Hummels et al. 2017), SYGMA (Ritter et al. 2018)

APPENDIX

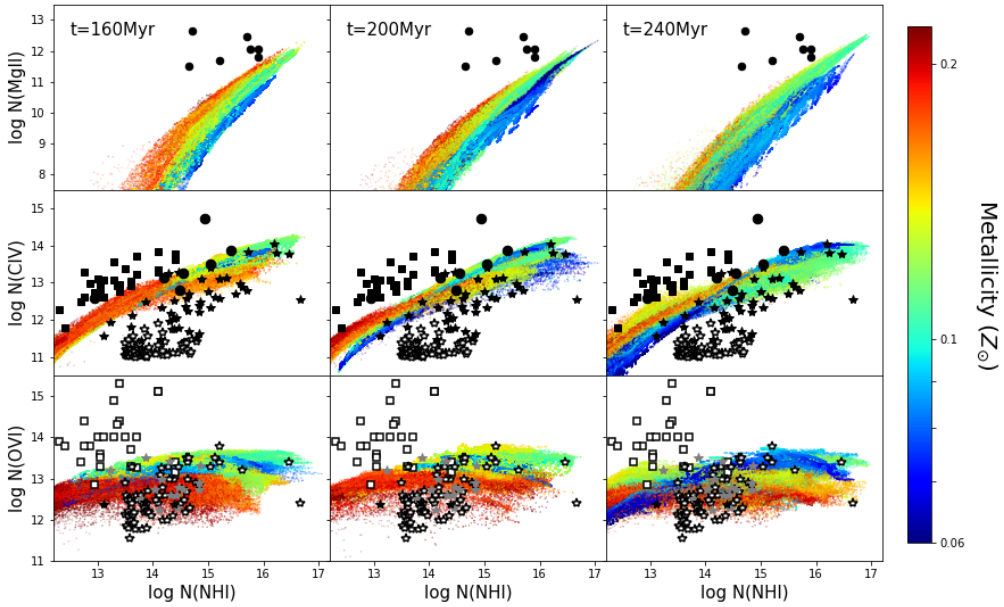


Figure 13. Same as Figure 9 for *low-res* simulation (25.6 pc)

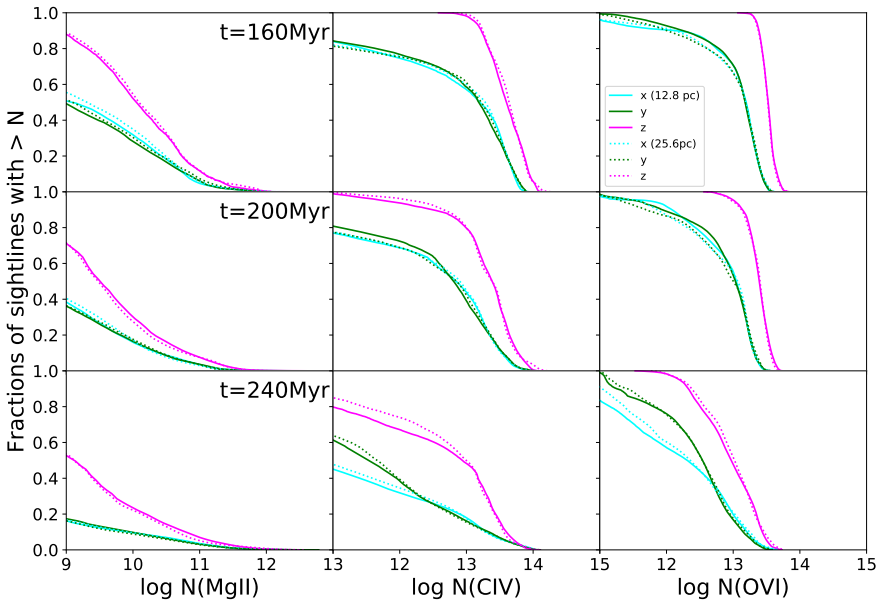


Figure 14. Same as Figure 10 but comparing the results in in our *standard* simulations (12.8 pc *solid*) and *low-res* simulation (25.6 pc *dashed*).

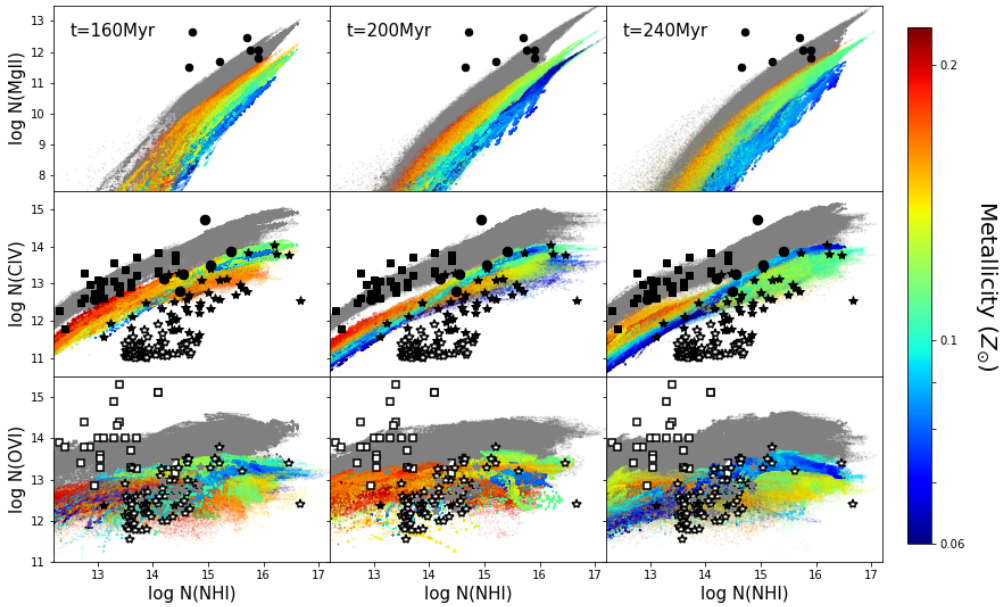


Figure 15. Same as Figure 9 but without overcooled gas ($n_H \leq 10^{-4}$ cm^{-3}, T$< 10^4$ K) in our *standard* simulation. The overcooled, low-density gas is metal-enriched outflow gas in region a. With or without it, there is very little change for MgII and CIV distributions, while there is a marginal difference in the distribution of higher metallicity OVI systems.

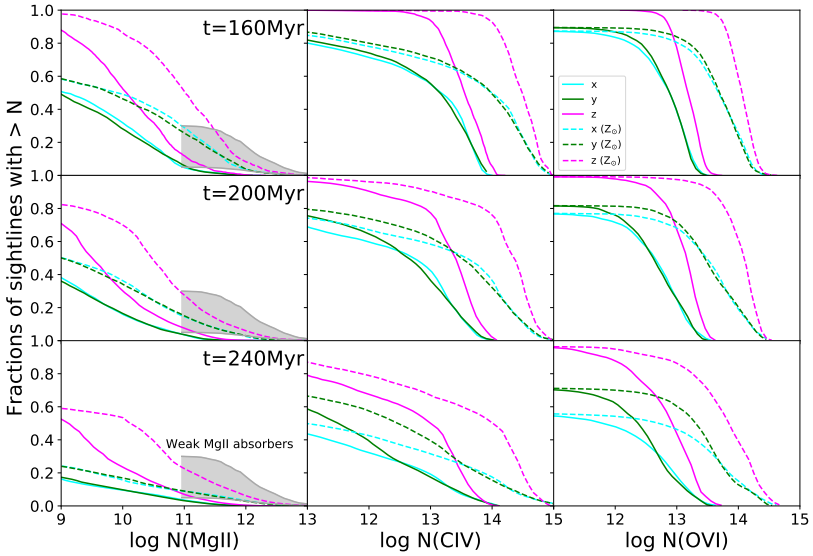


Figure 16. Same as Figure 9 but without overcooled gas ($n_H \leq 10^{-4}$ cm^{-3}, T$< 10^4$ K) in our *standard* simulation. With or without it, there is no noticeable difference in the covering fractions of MgII and CIV systems, but there is a slight decrease in the covering fraction of OVI systems at lower column density.

REFERENCES

Aghanim, N., Akrami, Y., & Ashdown, M. 2019, arXiv:1807.06209

Armillotto, L., Fraternali, F., & Marinacci, F. 2016, Monthly Notices of the Royal Astronomical Society, 462, 4157

Begelman, M. C. & Fabian, A. C. 1990, Monthly Notices of the Royal Astronomical Society, 244, 26

Bosman, S. E. I., Becker, G. D., Haehnelt, M. G., et al. 2017, Monthly Notices of the Royal Astronomical Society, 470, 1919

Bryan, G. L., Norman, M. L., O'Shea, B. W., et al. 2014, The Astrophysical Journal Supplement Series, 211, 19

Burkert, A. 1995, Astrophysical Journal Letters, 447, L25

Charlton, J. C., Ding, J., Zonak, S. G., et al. 2003, The Astrophysical Journal, 589

Codoreanu, A., Ryan-Weber, E. V., Crighton, N. H., et al. 2018, Monthly Notices of the Royal Astronomical Society, 472, 1023

Colella, P., & Woodward, P. R. 1984, Journal of Computational Physics, 54, 171

Cottle, J., Scannapieco, E., & Bruggen, M. 2018, The Astronomical Journal, 864

Ding, J., Charlton, J. C., & Churchill, C. W. 2005, Astrophysical Journal, 621, 612

D'Odorico, V., Cupani, G., Cristiani, S., et al. 2016, Monthly Notices of the Royal Astronomical Society, 463, 2690

Ferland, G. J., Porter, R. L., van Hoof, P. A. M., et al. 2013, Revista Mexicana de Astronomía y Astrofísica, 49, 137

Fujita, A., Martin, C. L., Mac Low, M.-M., New, K. C. B., & Weaver, R. 2009, ApJ, 698, 693 (F09)

Gronke, M., & Oh, S. P. 2018, MNRAS, 480, L111

—. 2020, MNRAS, 494, L27

Haardt, F., & Madau, P. 2012, The Astrophysical Journal, 746, 125

Heckman, T. M. 2017, Book chapter for 'Handbook of Supernovae' (arxiv:1701.09062), 47

Hummels, C. B., Smith, B. D., & Silvia, D. W. 2017, The Astrophysical Journal, 847, 17

Keating, L. C., Puchwein, E., Haehnelt, M. G., Bird, S., & Bolton, J. S. 2016, Monthly Notices of the Royal Astronomical Society, 461, 606

Kitsionas, S., Federrath, C., Klessen, R. S., et al. 2009, Astronomy & Astrophysics, 508, 541

Kritsuk, A. G., Norman, M. L., Padoan, P., & Wagner, R. 2007, The Astrophysical Journal, 665, 416

Kwak, K., & Shelton, R. L. 2010, The Astrophysical Journal, 719, 523

Lehner, N., O'Meara, J. M., Howk, J. C., Prochaska, J. X., & Fumagalli, M. 2016, The Astrophysical Journal, 833, 283

Lynch, R. S., & Charlton, J. C. 2007, The Astrophysical Journal, 666, 64

Mac Low, M.-M., & Zahnle, K. 1994, ApJL, 434, L33

Maio, U., Dolag, K., Ciardi, B., & Tornatore, L. 2007, Monthly Notices of the Royal Astronomical Society, 379, 963

McCourt, M., Oh, S. P., O'Leary, R., & Madigan, A.-M. 2018, MNRAS, 473, 5407

Milutinovic, N., Rigby, J. R., Masiero, J. R., et al. 2006, The Astrophysical Journal, 641, 190209

Misawa, T., Charlton, J. C., & Narayanan, A. 2008, The Astrophysical Journal, 679, 220

Mo, H. J., Mao, S., & White, S. D. M. 1998, Monthly Notices of the Royal Astronomical Society, 295, 319

Murray, S. G., C.Power, & A.S.G.Robotham. 2013, Astronomy and Computing, 3-4, 23

Muzahid, S., Fonseca, G., Roberts, A., et al. 2017, Monthly Notices of the Royal Astronomical Society

Narayanan, A., Charlton, J. C., Misawa, T., Green, R. E., & Kim, T.-S. 2008, The Astrophysical Journal, 689, 782

Navarro, J. F., Frenk, C. S., & White, S. D. M. 1997, ApJ, 490, 493

Oppenheimer, B. D., Dave, R., Katz, N., Kollmeier, J. A., & Weinberg, D. H. 2012, Monthly Notices of the Royal Astronomical Society, 420, 829

Oppenheimer, B. D., Schaye, J., Crain, R. A., Werk, J. K., & Richings, A. J. 2018, Monthly Notices of the Royal Astronomical Society, 481, 835

Peeples, M. S., Corlies, J., Tumlinson, J., et al. 2019, The Astrophysical Journal, 873

Rahmati, A., Pawlik, A. H., Raicevic, M., & Schaye, J. 2013, Monthly Notices of the Royal Astronomical Society, 430, 2427

Rigby, J. R., Charlton, J. C., & Chrchill, C. W. 2002, The Astrophysical Journal, 565, 743

Ritter, C., Cote, B., Herwig, F., Navarro, J. F., & Fryer, C. L. 2018, The Astrophysical Journal Supplement Series, 237, 42

Rose, A., & Bregman, J. N. 1995, ApJ, 440, 634

Schaye, J., Carswell, R. F., & Kim, T.-S. 2007, Monthly Notices of the Royal Astronomical Society, 379, 1169

Simcoe, R. A., Sargent, W. L. W., & Rauch, M. 2004, The Astrophysical Journal, 606, 92

Somerville, R. S., & Davé, R. 2015, ARA&A, 53, 51, doi: 10.1146/annurev-astro-082812-140951

Suresh, J., Bird, S., Vogelsberger, M., et al. 2015, Monthly Notices of the Royal Astronomical Society, 448, 895

Sutherland, R. S., & Dopita, M. A. 1993, ApJS, 88, 253

Tonnsen, S., & Bryan, G. L. 2009, The Astrophysical Journal, 694, 789

Toomre, A. 1963, ApJ, 138, 385. http://dx.doi.org/10.1086/147653

Turk, M. J., Smith, B. D., Oishi, J. S., et al. 2011, The Astrophysical Journal Supplement Series, 192, 9

Turner, M. L., Schaye, J., Crain, R. A., et al. 2017, Monthly Notices of the Royal Astronomical Society, 471, 690

Turner, M. L., Schaye, J., Steidel, C. C., Rudie, G. C., & Strom, A. L. 2014, Monthly Notices of the Royal Astronomical Society, 445, 794

—. 2015, Monthly Notices of the Royal Astronomical Society, 450

Waters, T., & Proga, D. 2019, ApJL, 876, L3

Weaver, R. W., McCray, R., Castor, J., Shapiro, P., & Moore, R. 1977, Astrophysical Journal, 218, 377